# Computational upper-limit of directional light emission in nano-LED via inverse design

## HAEJUN CHUNG* 

*Department of Electrical Engineering, Soongsil University, Seoul, 06978, Republic of Korea*
*haejun@ssu.ac.kr

**Abstract:** We demonstrate directional light emission in nano-LEDs using inverse design. Standard light-extraction strategies in LEDs have been limited to surface roughening or suppressing guided modes via LED structure modifications, which are insufficient for simultaneously achieving high-light extraction efficiency and directional emission. In this work, we use inverse design to discover high-efficiency directional emitting nano-LEDs. We first investigate the computational upper bounds of directional emission using free-form grayscale material, where material permittivity indicates an intermediate state between air and $SiO_2$. For a narrow emission angle ($<\pm30°$), the optimized grayscale design offers 4.99 times enhancement from the planar LED surface. Then, we apply fabrication constraints to our inverse design for discovering a single material ($SiO_2$) based design. The optimized $SiO_2$ surface design shows 4.71 times light extraction ($<\pm30°$) improvement compared with the planar configuration. This is a first theoretical demonstration of high light-extraction efficiency and directional emitting nano-LED designs.

## 1. Introduction

Modern light-emitting diodes (LEDs) offer nearly 100% internal quantum efficiency (IQE) with a cost-efficient and reliable manufacturing process [1,2]. However, unlike its IQE, micro/nano-LED's external quantum efficiency (EQE) is not close to ideal due to limited light-extraction efficiency (LEE) [3,4]. A planar surface between the LED-air interface causes total internal reflection (TIR), which restricts generated light escaping the LED structure [5–8]. Conventional approaches to address this issue include adding surface texturing [4,9,10] or modifying a LED structure which can eliminate a strong guided-mode [11–18], also in ultra-violet regime [19–21]. These approaches are generally successful in improving LEE, however, they often modify their emission angle close to the Lambertian radiation intensity [22]. This wide angle emission characteristic excludes applications in emerging sectors such as head-mounted displays, augmented reality glasses, projectors, and other display systems, which require directional light emission without sacrificing efficiency.

Alternative studies have suggested directional light emission from LEDs using aspheric lenses [23,24], external side walls [25], photonic crystals [26–31], Vogel spiral arrays [32], and optimized isotropic scattering arrays [33]. However, these approaches cannot be directly applicable to nano-LEDs where the LED size is comparable with the operating wavelength. Specifically, aspheric lenses are limited to a large LED due to their bulky, convex lens structure. Photonic crystal approaches also require a large surface area to secure multiple periods of photonic crystals. Non-periodic approaches such as Vogel spiral arrays and isotropic scattering arrays produce a ring shape in Fourier space, successfully suppressing higher-angle emissions in real space. However, these approaches are also unsuitable for nano-scale LEDs because designing such arrays within one or two $\lambda$-size LEDs is unfeasible. On the other hand, the evanescent wave-coupler method, where the triangular LED cavity is used, successfully achieves directional emission. However, their measured EQE is only 4% due to strong light confinement in the metallic structure [34].

As an LED size approaches its operating wavelength, it starts to suffer an additional challenge, i.e., strong parasitic absorption at the metallic wall [35]. Thus, in nano-LED designs, eliminating a guide mode that increases parasitic absorption could be essential. In this work, we apply photonic inverse design to discover novel nano-LED designs that simultaneously achieve high-LEE and directional emissions while suppressing guided modes in the cubical LED structure. Inverse design, a large-scale computational optimization technique, has demonstrated revolutionary outcomes in areas such as metasurface [36–38], beam deflector [39–41], solar cells [42], and others [43,44]. In only two simulations, inverse design, often called adjoint optimization, can efficiently calculate the gradient of a figure of merit function for all design parameters.

Our work is organized as follows: numerical modeling of a randomly polarized light emission process in nano-LEDs is studied in Sec. 2. Then we discuss our inverse design approach for optimizing nano-LED surface designs in the same section. In Sec. 3., we first investigate a computational maximum LEE with grayscale material which is a theoretical material that can have a middle state between two materials. Then, we apply the penalization technique to make this middle state material binary consisting of $SiO_2$ and air. Finally, in Sec. 4., we summarize our work and discuss the potential outlook for future nano-LED designs which can have both high-efficiency and directional emission.

## 2. Nano-LED inverse design framework

The most straightforward nano-LED structure may consist of Multi-Quantum Well (MQW) and n, p-type materials (GaN) encapsulated by metallic walls ($Al_2O_3$) [3,45]. Doped-GaN materials have a slight change in their refractive indices depending on their doping concentrations [46]. We treat p, n, i-type GaN with the same refractive indices in this work since the small variation of refractive indices ($\Delta n$) could be negligible in optical simulations because optical path length change is less than $\Delta n \times L/\lambda < 0.01$. As shown in Fig. 1(a), this type of nano-LEDs undergoes TIR at the air and the LED interface as well as significant guided modes which create strong parasitic absorption at the metallic walls, and eventually results in low LEE. A typical improvement to the planar surface is to roughen the LED surface to couple guided modes to air [5,22,47]. This approach is generally successful, as shown in Fig. 1(b). However, roughening LED surface substantially modifies emission angles to Lambertian distribution, where only 50% of the escaping light has a narrow emission angle ($<\pm30°$). Thus, in this work, we aim to discover a surface structure that can simultaneously have narrow emission characteristics and high-efficiency, as shown in Fig. 1(c).

Modeling random fluctuation of incoherent emitting photons in simulations is challenging due to a computational burden. One way of modeling incoherent light emission process is to introduce uncorrelated white-noise sources into the computation of Maxwell's equation [48,49] or using trace formulation [50]. In this work, instead of simulating multiple dipoles at a time, which may create a non-physical interference pattern due to coherent dipole sources [51], we directly simulate each polarization and each location of dipole excited at the QW one by one and then average them to obtain the angle-dependent emissivity. This approach is computationally inefficient, but it is relatively feasible for nano-LEDs where the QW width is less than a few wavelengths. This work employs the finite-difference time-domain (FDTD) method, which solves Maxwell's equations over time and space. To compute the incidence power of the dipoles in FDTD, we place flux monitors, which surround the dipole source, and then accumulate electromagnetic fluxes passing through them over simulation time. The escaping angle is approximated at the one $\lambda$ atop from the LED surface with planewave mode decomposition [52]. For an electric field at the planewave monitor (red dashed line in Fig. 2(a)) is given by

$$E(x) = \frac{1}{A} \sum_i \sum_j c_{ij} \hat{\varepsilon}_j \exp(i k_i \cdot x), \tag{1}$$
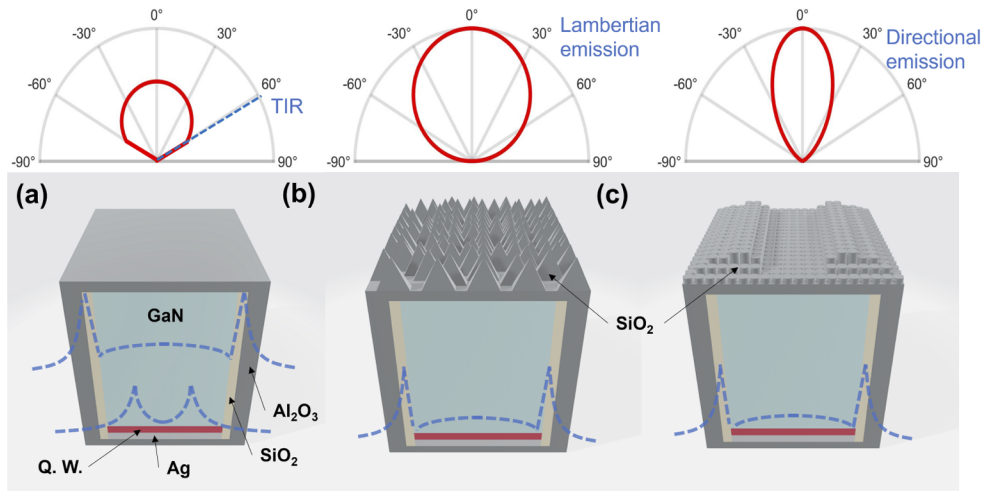
**Fig. 1.** Schematic drawing of nano-LED designs. (a) Planar surface-based nano-LEDs have a total internal reflection at the interface between air and nano-LEDs, significantly reducing light extraction efficiency. The blue dashed curves indicate guided modes. The red curves in the polar plot show emission intensity. (b) Roughening the nano-LED surface improves light extraction efficiency, but it modifies emission angle close to Lambertian distribution. (c) Inverse design can discover a surface design that simultaneously have narrow emission characteristics and a superior light extraction efficiency. Two-dimensional GaN-based nano-LED is assumed in this study. The sidewall has a 100-nm-thick aluminum oxide with 70-nm-thick SiO$_2$ for reducing surface recombination loss.

where $A$ is the area of the planewave monitor, $i$ and $j$ are a discretized order indicating angle and polarization, $\mathbf{k}_i$ is the wavevector of each plane wave, $\hat{\boldsymbol{\varepsilon}}_j$ is the polarization unit-vector, and $c_{ij}$ is a coefficient of the planewave mode which has $\mathbf{k}_i$ and $\hat{\boldsymbol{\varepsilon}}_j$. Once the electric field at the planewave monitor is decomposed, we can approximate the escaping angle of the incidence dipole. The angle-dependent LEE is then calculated via

$$\eta(\theta_i) = P_i/P_{in}, \tag{2}$$

where $P_{in}$ is incident power calculated by the flux monitors surrounding the dipole, and $P_i$ is a calculated power of the $i_{th}$ planewave mode. The planewave mode decomposition significantly reduces the computational cost of the simulation; however the accuracy of the mode decomposition may depend on the number of the mode we define. Therefore, we validate our approach against far-field field intensity at $20\lambda$ above from the LED surface, as shown in Fig. 2. Three dipoles at an arbitrary location in the QW are excited separately. Then, we compare the far-field angular intensity distribution against the mode decomposition result, which is performed one $\lambda$ above the LED surface. Figure 2(b)-(d) show their validation, which reveals fairly good agreement. Note that the optimum structures in this work are always validated with the far-field intensity distribution while the mode decomposition is used for calculating the figure of merits during the inverse design process.

We define our figure of merit as follows:

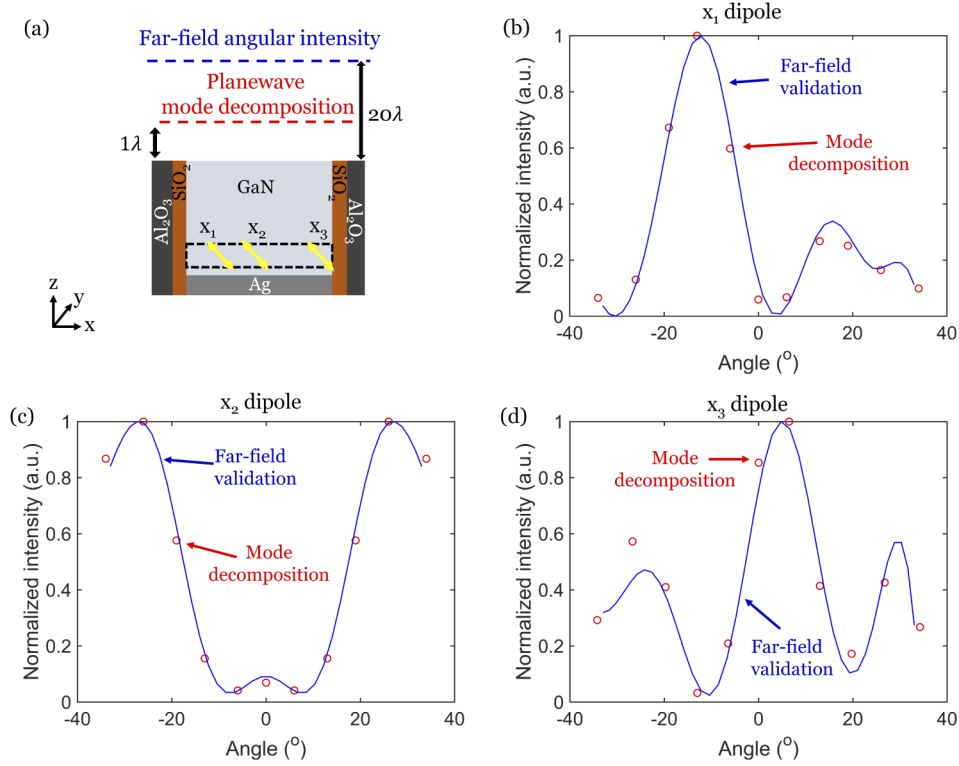$$\mathcal{F} = \frac{1}{2}\sum_i\sum_j |c_{i,j}^* c_{i,j}^{tar}|^2, \tag{3}$$

**Fig. 2.** Schematic diagram of the nano-LED simulation. (a) Electric fields are calculated at $1\lambda$ above (planewave monitor) and at $20\lambda$ (far-field monitor). Then, the electric fields calculated in the planewave monitor are converted to a far-field angular field distribution using planewave mode decomposition [52]. To validate angular distribution calculated by two monitors, three random dipoles [$x_1$ (b), $x_2$ (c), and $x_3$ (d)] are tested in independent simulations.

where $c_{i,j}^{\text{tar}}$ is a target coefficient for the planewave mode which has $\boldsymbol{k}_i$ and $\hat{\boldsymbol{\varepsilon}}_j$, and the asterisk denotes complex conjugation. $c_{i,j}^{\text{tar}}$ is set to zero for a planewave angle greater than $\pm 30°$, while the other coefficients are set to ideal.

The efficient computation of the gradient with respect to the possible geometrical degrees of freedom is a fundamental step in inverse design. Instead of simulating each geometrical perturbation separately, one can apply a series of single coherent sources with an amplitude determined by the variation of the figure of merit to calculate "adjoint" field [53] that provides information about every possible perturbation in a single FDTD simulation [54]. The adjoint current sources ($\boldsymbol{J}_{\text{adj}}$) are given by [53]:

$$
\begin{aligned}
\boldsymbol{J}_{\text{adj}}(x) &= -i\omega \boldsymbol{P}_{\text{adj}} \\
&= -i\omega \frac{\partial \mathcal{F}}{\partial \boldsymbol{E}} \\
&= -i\omega \sum_i \sum_j \frac{\partial \mathcal{F}}{\partial c_{i,j}} \frac{\partial c_{i,j}}{\partial \boldsymbol{E}} \\
&= \frac{-i\omega}{A} \sum_i \sum_j \frac{\partial \mathcal{F}}{\partial c_{i,j}} \hat{\boldsymbol{\varepsilon}}_j \exp(i\boldsymbol{k}_i \cdot \boldsymbol{x}).
\end{aligned}
\tag{4}
$$

The adjoint sources are time-reversed plane wave modes which have a weighted amplitude and phase calculated via Eq. (4). This has the same root as "error backpropagation" in deep-learning neural networks [55,56]. The adjoint optimization procedure is as follows: first, we simulate an incidence dipole at each polarization and each location of the QW independently. For each simulation, we compute $J_{adj}$ at the planewave monitor and then run the adjoint simulation with the adjoint source. Two simulations (direct and adjoint) now give information regarding $\partial \mathcal{F}$ for all geometric Degree of Freedoms (DoF). We then average over the $\partial \mathcal{F}$s obtained by independent dipole simulations. To update DoF (LED surface in this work), $\partial \mathcal{F}/\partial \varepsilon(\boldsymbol{x})$, the gradient of $\mathcal{F}$ with respect to dielectric permittivity perturbations, should be computed via $\partial \mathcal{F}/\partial \varepsilon(\boldsymbol{x}) = \text{Re}\left[\boldsymbol{E}(\boldsymbol{x}) \cdot \boldsymbol{E}_{adj}(\boldsymbol{x})\right]$. To discover an ideal design, these derivatives can be employed in gradient descent [57,58] or other nonlinear optimization methods [59,60], where we apply gradient descent in this work for simplicity. We simulate nano-LED structures with Meep, an open-source software package for FDTD simulations [61]. Meep is especially powerful for a large-scale simulation due to its subpixel smoothing technique [62] and efficient parallelization. We focus on a 1,000nm-width nano-LED design at 450nm wavelength in this work, but the proposed method can be directly applicable to other visible wavelengths and other materials. We validate numerical stability and convergence of our final design with a few different simulation resolutions. Although simulating an infinite number of independent dipoles over the QW regime would be ideal, we discretize the QW regime with 20nm pixels to reduce the computational burden for calculating the light-extraction efficiency of the nano-LED. We validated that any smaller pixel size than 20nm does not create a significantly accurate approximation. Also, we validate convergence of simulations with much fine grid spacing for the optimized nano-LEDs. Each iteration of the adjoint optimization takes 300 FDTD simulations due to averaging over spatially distributed dipoles' responses. In our 25-core computational cluster (Intel Xeon E5-2660 v4 3.2 GHz processors), each simulation takes less than 10 seconds.

## 3. Directional emitting nano-LED design

In this section, we design a nano-LED operating at 450nm wavelength with both high-LEE and directional emission. We assume two-dimensional LED structures with a QW width of 1,000nm and a 70-nm-passivation layer with $SiO_2$ and 100-nm-thick aluminum oxide at the side, as shown in Fig. 3(a). We employ commonly used materials in nano, micro-LED designs for a simple implementation. Material permittivities used in this work are chosen as $SiO_2 = 2.13$ [63], Ag= $-7.01 + i0.21$ [64], GaN=6.18 [65], and $Al_2O_3$ =3.17 [64]. Complex permittivities of materials are simulated by setting the conductivity $\sigma D$ in MEEP [61]. The back reflector is silver in this work. Independent simulations with different polarization (x,y,z) and pixel location (20nm distance) are performed; then, their angle-dependent LEEs are calculated at the planewave monitor which is indicated in Fig. 3(a) as a red dashed line. The perfectly matched layer boundary condition is used on all boundary conditions.

### 3.1. High-efficiency directional nano-LED via grayscale freeform design

This subsection demonstrates a high-efficiency directional emitting nano-LED design using grayscale material where material permittivity indicates intermediate state between air and high-permittivity material. In this method, we can thoroughly investigate the physical bound of this design problem due to greater DoFs combined with multiple materials and free-form structures. As shown in Fig. 3(b), the initial nano-LED design (planar surface) achieves an average LEE of 29.69% for entire escaping angles, while LEE within ±30° is only 8.35%. This LEE (±30°) is surprisingly low compared to a typical Lambertian emission where 50% of light extraction falls into the ±30° escape cone. We presume that intense guided modes in the nano-LED structure cause this wide emission characteristic in the initial structure. Any surface roughening or eliminating guided modes via LED structure modification may improve this initial
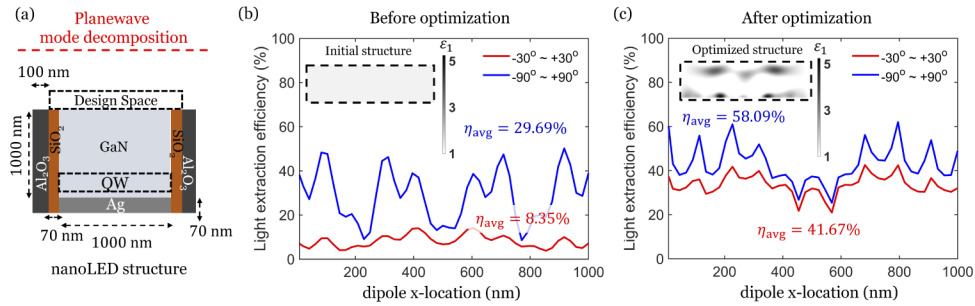
**Fig. 3.** (a) Cross-section schematic of the inverse-designed nano-LED. The side wall has a 100-nm-thick aluminum oxide with 70-nm-thick $SiO_2$ for reducing surface recombination loss. InGaN/GaN QW is assumed as an active region where the injected electricity is converted to photon emission. The back reflector is Ag while the nano-LED cavity is composed of GaN. $SiO_2$ is used for design space where the inverse design discovers the optimal design. (b) Light Extraction Efficiency (LEE) calculated for different polarization (x,y,z) and emission locations with the initial planar surface. The red curve indicates LEE within an escape angle of $\pm 30°$; the blue curve indicates LEE over whole angles. The average LEE within $\pm 30°$ escape angles is 8.35% in the initial geometry. (c) LEE calculated with optimized grayscale geometry. The optimized structure shows average LEE of 41.67% within $\pm 30°$ escape angles, which corresponds to 4.99 times improvement.

result close to Lambertian emission. Here, we apply the inverse design technique to improve its emission angle and LEE. Figure 3(c) shows an optimized nano-LED surface design with a grayscale material. The averaged LEE (averaging over spatial dipoles at the QW regime) is 58.90% for a $\pm 90°$ escape cone, while directional emission ($\pm 30°$ escape cone) is 41.67% which demonstrates roughly 4.99 times improvement compared with the initial structure. This result potentially indicates a computational maximum LEE, which may also be close to the physical limit of directional emission in the given device dimension as we previously demonstrated in existing inverse design works [52,66], where their inverse designed metasurfaces show efficiencies close to their physical bounds. However, the optimized structure shown in the inset of Fig. 3(c) does not look feasible for realization due to free-standing objects and variation of permittivity over space. Therefore, in the following subsection, we employ a penalization method in the inverse design steps so that the final structure only includes two materials (air, $SiO_2$).

### 3.2. High-efficiency directional nano-LED via a binary design

In this subsection, we allow the density of $SiO_2$ in the design space to vary between zero and one at every point in it, which is often called "topology optimization" [68–70]. Thus, a position-dependent permittivity function can be given by $\varepsilon_r = \varepsilon_{air} + \zeta(\varepsilon_{SiO2} - \varepsilon_{air})$, where $\zeta \in [0,1]$ is a relaxation parameter. Once our adjoint optimization finds the highest figure of merit during its iterations, as shown in Fig. 4(a), the penalization function, which gradually increases over the iterations, enforces a binary-material constraint by adding a penalization factor to the gradient of the figure of merit ($\partial \mathcal{F}$) [53]. Figure 4(a) shows rapid increase of the $\pm 30°$ LEE until $37_{th}$ iteration with grayscale permittivities. After the penalization factor kicks in, the $\pm 30°$ LEE slightly decreases while the combination $\partial \mathcal{F}$ and penalization factor discovers a relatively high-performance design only consisting of $SiO_2$ as indicated in the inset figure in the blue dashed area in Fig. 4(a). The LEE decrement due to the binary conversion is only 1.76%, which can be marginal compared with the improvement of our optimum design. As shown in Fig. 4(b), our optimized $SiO_2$ based surface design demonstrates 56.80% LEE for entire escaping angles with 39.31% LEE for the directional emission ($\pm 30°$). This result corresponds

4.71 times improvement compared with the initial structure shown in Fig. 3(b); it also reaches 94.34% relative performance to the optimum grayscale design shown in Fig. 3(c). This is a first demonstration of the inverse design method in directional nano-LED designs where it can be extended to different wavelengths via a scale-invariant characteristic of Maxwell's equations. Table 1 shows a comparison among the existing directional emission studies [3,13,67] and this work. Our optimized nano-LEDs shows superior directional emission as well as high-LEEs. Although we optimize two-dimensional nano-LEDs in a single node computer, our approach is directly applicable to three-dimensional nano-LEDs with a multi-node computational cluster. We can further simplify the final design shown in Fig. 4 by imposing fabrication constraints such as a translational symmetry over the z-direction [52,71]. We expect substantial efforts for minimizing

**Table 1. Comparison among the existing directional emission studies [3,13,67] and this work. Active layers are InGaN/GaN for all references. I30°/I90° indicates the intensity ratio between narrow emission (±30°) and all angle emission (±90°). Note that some references reporting high-directional emission but very low light extraction efficiency are not included here.**

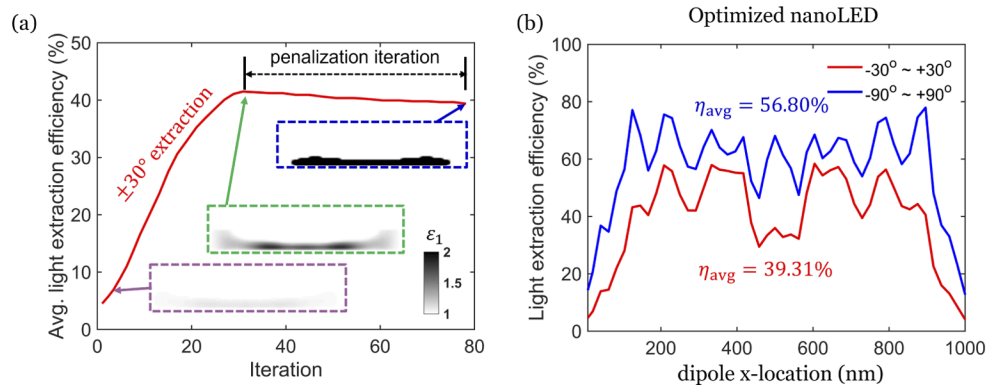| Wavelength (nm) | Device width ($\mu$m) | Design (material) | I30° / I90° | Ref. |
|---|---|---|---|---|
| 500 | NA | Planar ($SiO_2$) | 0.38 | [67] |
| 500 | 0.5 | Sphere ($SiO_2$) | 0.53 | [67] |
| 500 | 0.5 | Sphere (Antase $TiO_2$) | 0.42 | [67] |
| 500 | 0.5 | Sphere (a-$TiO_2$) | 0.54 | [67] |
| 455 | 2.0 | Rough (Sapphire sub.) | 0.49 | [3] |
| 455 | 2.0 | Smooth (Sapphire sub.) | 0.58 | [3] |
| 460 | NA | Planar (GaN) | 0.42 | [13] |
| 460 | 0.1–0.25 | Nano-rod (GaN) | 0.53 | [13] |
| 450 | 1.0 | Free-form (Grayscale) | 0.72 | This work |
| 450 | 1.0 | Free-form ($SiO_2$) | 0.69 | This work |



**Fig. 4.** $SiO_2$ based nano-LED surface design. (a) Averaged Light Extraction Efficiency (LEE) within ±30° escape angles over the inverse design iterations. Until the average LEE saturates, the design space evolves with grayscale, which can have a dielectric constant between $SiO_2$ and air. Then, the penalization kicks in to binarize grayscale geometry to $SiO_2$. (b) LEE for all angle emissions (blue curve) is 56.80% (1.91 times improvement from the planar geometry), while LEE for directional emission (±30°) is 39.31% (4.71 times improvement from the planar geometry).

device performance degradation due to fabrication imperfection. Toward this purpose, one can apply a robustness-control algorithm [72,73] during the inverse design process to decouple a fabrication error and the device performance. Then, one may apply a fabrication constraint specific to the manufacturer's requirements, which closes the gap between a computational design and a fabrication.

## 4.   Conclusion

In this work, we have demonstrated a nano-LED design framework for achieving high-efficiency directional emitting nano-LEDs. We focused on a two-dimensional structure to allow rapid systematic design of nano-LED systems, covering variation of light-extraction efficiencies over spatial dipole emissions. We have validated our planewave mode decomposition method, which significantly reduces computational costs by approximating emission angles at the near field. We also discovered high-efficiency directional emitting nano-LEDs with grayscale and binary material at the 450 nm wavelength through inverse design. This is a first theoretical demonstration of high light extraction efficiency and directional emitting nano-LED designs. Unlike conventional approaches, where random texturing or human-intuition-based physical designs have been applied, we apply an inverse design to discover high-performance designs. The inverse design calculates derivatives of a figure of merit with only two simulations. Thus, it enables us to discover optimum designs in a few tens of iterations. This framework may pave the way for realizing future nano-LED, which can significantly contribute to the commercialization of augmented reality applications and optical communications.

## 5.  Appendix:Geometry parameters

Raw permittivity data of the finalized nano-LED surface design is shown in Table 2. The permittivity of 2.13 indicates $SiO_2$ while 1.00 indicates air in Table 2. The column indices indicate the x-axis and the row indices indicate the z-axis.

**Table  2.  Design parameters for Fig. 4.**

| index | z=1 | 2 | 3 | 4 | 5 |
|-------|-----|------|------|------|------|
| x=1 | 1.00 | 1.00 | 2.13 | 1.00 | 1.00 |
| 2 | 1.00 | 2.13 | 2.13 | 1.00 | 1.00 |
| 3 | 1.00 | 2.13 | 2.13 | 1.00 | 1.00 |
| 4 | 2.13 | 2.13 | 2.13 | 2.13 | 1.00 |
| 5 | 2.13 | 2.13 | 2.13 | 2.13 | 1.00 |
| 6 | 2.13 | 2.13 | 2.13 | 2.13 | 1.00 |
| 7 | 2.13 | 2.13 | 2.13 | 2.13 | 1.00 |
| 8 | 2.13 | 2.13 | 2.13 | 2.13 | 1.00 |
| 9 | 2.13 | 2.13 | 2.13 | 2.13 | 2.13 |
| 10 | 2.13 | 2.13 | 2.13 | 2.13 | 2.13 |
| 11 | 2.13 | 2.13 | 2.13 | 2.13 | 2.13 |
| 12 | 2.13 | 2.13 | 2.13 | 2.13 | 2.13 |
| 13 | 2.13 | 2.13 | 2.13 | 2.13 | 2.13 |
| 14 | 2.13 | 2.13 | 2.13 | 2.13 | 1.00 |
| 15 | 2.13 | 2.13 | 2.13 | 2.13 | 1.00 |
| 16 | 2.13 | 2.13 | 2.13 | 2.13 | 1.00 |
| 17 | 2.13 | 2.13 | 2.13 | 2.13 | 1.00 |

| index | z=1 | 2 | 3 | 4 | 5 |
|-------|------|------|------|------|------|
| 18 | 2.13 | 2.13 | 2.13 | 2.13 | 1.00 |
| 19 | 2.13 | 2.13 | 2.13 | 2.13 | 1.00 |
| 20 | 2.13 | 2.13 | 2.13 | 2.13 | 1.00 |
| 21 | 2.13 | 2.13 | 2.13 | 2.13 | 1.00 |
| 22 | 2.13 | 2.13 | 2.13 | 2.13 | 1.00 |
| 23 | 2.13 | 2.13 | 2.13 | 1.00 | 1.00 |
| 24 | 2.13 | 2.13 | 2.13 | 1.00 | 1.00 |
| 25 | 2.13 | 2.13 | 2.13 | 1.00 | 1.00 |
| 26 | 2.13 | 2.13 | 2.13 | 1.00 | 1.00 |
| 27 | 2.13 | 2.13 | 2.13 | 1.00 | 1.00 |
| 28 | 2.13 | 2.13 | 2.13 | 1.00 | 1.00 |
| 29 | 2.13 | 2.13 | 2.13 | 1.00 | 1.00 |
| 30 | 2.13 | 2.13 | 2.13 | 1.00 | 1.00 |
| 31 | 2.13 | 2.13 | 2.13 | 1.00 | 1.00 |
| 32 | 2.13 | 2.13 | 2.13 | 1.00 | 1.00 |
| 33 | 2.13 | 2.13 | 2.13 | 1.00 | 1.00 |
| 34 | 2.13 | 2.13 | 2.13 | 1.00 | 1.00 |
| 35 | 2.13 | 2.13 | 2.13 | 1.00 | 1.00 |
| 36 | 2.13 | 2.13 | 2.13 | 1.00 | 1.00 |
| 37 | 2.13 | 2.13 | 2.13 | 1.00 | 1.00 |
| 38 | 2.13 | 2.13 | 2.13 | 1.00 | 1.00 |
| 39 | 2.13 | 2.13 | 2.13 | 1.00 | 1.00 |
| 40 | 2.13 | 2.13 | 2.13 | 1.00 | 1.00 |
| 41 | 2.13 | 2.13 | 2.13 | 1.00 | 1.00 |
| 42 | 2.13 | 2.13 | 2.13 | 1.00 | 1.00 |
| 43 | 2.13 | 2.13 | 2.13 | 1.00 | 1.00 |
| 44 | 2.13 | 2.13 | 2.13 | 1.00 | 1.00 |
| 45 | 2.13 | 2.13 | 2.13 | 1.00 | 1.00 |
| 46 | 2.13 | 2.13 | 2.13 | 1.00 | 1.00 |
| 47 | 2.13 | 2.13 | 2.13 | 1.00 | 1.00 |
| 48 | 2.13 | 2.13 | 2.13 | 1.00 | 1.00 |
| 49 | 2.13 | 2.13 | 2.13 | 1.00 | 1.00 |
| 50 | 2.13 | 2.13 | 2.13 | 1.00 | 1.00 |
| 51 | 2.13 | 2.13 | 2.13 | 1.00 | 1.00 |
| 52 | 2.13 | 2.13 | 2.13 | 2.13 | 1.00 |
| 53 | 2.13 | 2.13 | 2.13 | 2.13 | 1.00 |
| 54 | 2.13 | 2.13 | 2.13 | 2.13 | 1.00 |
| 55 | 2.13 | 2.13 | 2.13 | 2.13 | 1.00 |
| 56 | 2.13 | 2.13 | 2.13 | 2.13 | 1.00 |
| 57 | 2.13 | 2.13 | 2.13 | 2.13 | 1.00 |
| 58 | 2.13 | 2.13 | 2.13 | 2.13 | 1.00 |
| 59 | 2.13 | 2.13 | 2.13 | 2.13 | 1.00 |

| index | z=1 | 2 | 3 | 4 | 5 |
|-------|------|------|------|------|------|
| 60 | 2.13 | 2.13 | 2.13 | 2.13 | 1.00 |
| 61 | 2.13 | 2.13 | 2.13 | 2.13 | 2.13 |
| 62 | 2.13 | 2.13 | 2.13 | 2.13 | 2.13 |
| 63 | 2.13 | 2.13 | 2.13 | 2.13 | 2.13 |
| 64 | 2.13 | 2.13 | 2.13 | 2.13 | 2.13 |
| 65 | 2.13 | 2.13 | 2.13 | 2.13 | 2.13 |
| 66 | 2.13 | 2.13 | 2.13 | 2.13 | 1.00 |
| 67 | 2.13 | 2.13 | 2.13 | 2.13 | 1.00 |
| 68 | 2.13 | 2.13 | 2.13 | 2.13 | 1.00 |
| 69 | 2.13 | 2.13 | 2.13 | 2.13 | 1.00 |
| 70 | 2.13 | 2.13 | 2.13 | 2.13 | 1.00 |
| 71 | 1.00 | 2.13 | 2.13 | 1.00 | 1.00 |
| 72 | 1.00 | 2.13 | 2.13 | 1.00 | 1.00 |
| 73 | 1.00 | 1.00 | 2.13 | 1.00 | 1.00 |

## 6. Appendix:Material parameters

Complex permittivity data of the nano-LED materials used in this work at 450 nm wavelength is shown in Table 3.

**Table 3. Complex permittivity of the nano-LED materials used in this work at 450 nm wavelength.**

| Material | Complex permittivity | Ref. |
|----------|---------------------|------|
| $SiO_2$ | 2.13 | [63] |
| Ag | $-7.01 + i0.21$ | [64] |
| GaN | 6.18 | [65] |
| $Al_2O_3$ | 3.17 | [64] |

**Disclosures.** The authors declare no conflicts of interest.

**Data availability.** Data underlying the results presented in this paper are available in Appendix section. Also, they may be obtained from the author upon reasonable request.

## References

1. H. Zhao, G. Liu, J. Zhang, R. A. Arif, and N. Tansu, "Analysis of internal quantum efficiency and current injection efficiency in iii-nitride light-emitting diodes," J. Disp. Technol. **9**(4), 212–225 (2013).
2. P. Kivisaari, L. Riuttanen, J. Oksanen, S. Suihkonen, M. Ali, H. Lipsanen, and J. Tulkki, "Electrical measurement of internal quantum efficiency and extraction efficiency of iii-n light-emitting diodes," Appl. Phys. Lett. **101**(2), 021113 (2012).
3. R. T. Ley, J. M. Smith, M. S. Wong, T. Margalith, S. Nakamura, S. P. DenBaars, and M. J. Gordon, "Revealing the importance of light extraction efficiency in ingan/gan microleds via chemical treatment and dielectric passivation," Appl. Phys. Lett. **116**(25), 251104 (2020).
4. T. Wei, Q. Kong, J. Wang, J. Li, Y. Zeng, G. Wang, J. Li, Y. Liao, and F. Yi, "Improving light extraction of ingan-based light emitting diodes with a roughened p-gan surface using cscl nano-islands," Opt. Express **19**(2), 1065–1071 (2011).

5.  T.-X. Lee, K.-F. Gao, W.-T. Chien, and C.-C. Sun, "Light extraction analysis of gan-based light-emitting diodes with surface texture and/or patterned substrate," Opt. Express **15**(11), 6670–6676 (2007).

6.  P. Zhao and H. Zhao, "Analysis of light extraction efficiency enhancement for thin-film-flip-chip ingan quantum wells light-emitting diodes with gan micro-domes," Opt. Express **20**(S5), A765–A776 (2012).

7.  N. Li, K. Liu, V. J. Sorger, and D. K. Sadana, "Monolithic iii–v on silicon plasmonic nanolaser structure for optical interconnects," Sci. Rep. **5**(1), 14067 (2015).

8.  K. Saxena, V. Jain, and D. S. Mehta, "A review on the light extraction techniques in organic electroluminescent devices," Opt. Mater. **32**(1), 221–233 (2009).

9.  H. Jeong, D. J. Park, H. S. Lee, Y. H. Ko, J. S. Yu, S.-B. Choi, D.-S. Lee, E.-K. Suh, and M. S. Jeong, "Light-extraction enhancement of a gan-based led covered with zno nanorod arrays," Nanoscale **6**(8), 4371–4378 (2014).

10. X.-H. Li, R. Song, Y.-K. Ee, P. Kumnorkaew, J. F. Gilchrist, and N. Tansu, "Light extraction efficiency and radiation patterns of iii-nitride light-emitting diodes with colloidal microlens arrays with various aspect ratios," IEEE Photonics J. **3**(3), 489–499 (2011).

11. S. Kim, J. M. Shin, J. Lee, C. Park, S. Lee, J. Park, D. Seo, S. Park, C. Y. Park, and M. S. Jang, "Inverse design of organic light-emitting diode structure based on deep neural networks," Nanophotonics **10**(18), 4533–4541 (2021).

12. N. M. Andrade, S. Hooten, S. A. Fortuna, K. Han, E. Yablonovitch, and M. C. Wu, "Inverse design optimization for efficient coupling of an electrically injected optical antenna-led to a single-mode waveguide," Opt. Express **27**(14), 19802–19814 (2019).

13. M.-L. Kuo, Y.-J. Lee, T. C. Shen, and S.-Y. Lin, "Large enhancement of light-extraction efficiency from optically pumped, nanorod light-emitting diodes," Opt. Lett. **34**(13), 2078–2080 (2009).

14. J. Zhu, L. Wang, S. Zhang, H. Wang, D. Zhao, J. Zhu, Z. Liu, D. Jiang, and H. Yang, "The fabrication of gan-based nanopillar light-emitting diodes," J. Appl. Phys. **108**(7), 074302 (2010).

15. S. Li and A. Waag, "Gan based nanorods for solid state lighting," J. Appl. Phys. **111**(7), 071101 (2012).

16. B. Romeira and A. Fiore, "Physical limits of nanoleds and nanolasers for optical communications," Proc. IEEE **108**(5), 735–748 (2020).

17. M.-L. Kuo, Y.-S. Kim, M.-L. Hsieh, and S.-Y. Lin, "Efficient and directed nano-led emission by a complete elimination of transverse-electric guided modes," Nano Lett. **11**(2), 476–481 (2011).

18. Q. Wang, J. Bai, Y. Gong, and T. Wang, "Influence of strain relaxation on the optical properties of ingan/gan multiple quantum well nanorods," J. Phys. D: Appl. Phys. **44**(39), 395102 (2011).

19. B. Jain, R. T. Velpula, M. Tumuna, H. Q. T. Bui, J. Jude, T. T. Pham, A. V. Hoang, R. Wang, and H. P. T. Nguyen, "Enhancing the light extraction efficiency of alinn nanowire ultraviolet light-emitting diodes with photonic crystal structures," Opt. Express **28**(15), 22908–22918 (2020).

20. R. Floyd, M. Gaevski, K. Hussain, A. Mamun, M. Chandrashekhar, G. Simin, and A. Khan, "Enhanced light extraction efficiency of micropixel geometry algan duv light-emitting diodes," Appl. Phys. Express **14**(8), 084002 (2021).

21. M. Patel, B. Jain, R. T. Velpula, and H. P. T. Nguyen, "Effect of hfo2 passivation layer on light extraction efficiency of alinn nanowire ultraviolet light-emitting diodes," ECS Trans. **102**(3), 35–42 (2021).

22. S. Fahr, T. Kirchartz, C. Rockstuhl, and F. Lederer, "Approaching the lambertian limit in randomly textured thin-film solar cells," Opt. Express **19**(S4), A865–A874 (2011).

23. A. Cvetkovic, O. Dross, J. Chaves, P. Benitez, J. C. Mi nano, and R. Mohedano, "Etendue-preserving mixing and projection optics for high-luminance leds, applied to automotive headlamps," Opt. Express **14**(26), 13014–13020 (2006).

24. A. Wilm, "Requirements on leds in etendue limited light engines," in *Photonics in Multimedia II*, vol. 7001 (International Society for Optics and Photonics, 2008), p. 70010F.

25. H.-Y. Lin, C.-W. Sher, D.-H. Hsieh, X.-Y. Chen, H.-M. P. Chen, T.-M. Chen, K.-M. Lau, C.-H. Chen, C.-C. Lin, and H.-C. Kuo, "Optical cross-talk reduction in a quantum-dot-based full-color micro-light-emitting-diode display by a lithographic-fabricated photoresist mold," Photonics Res. **5**(5), 411–416 (2017).

26. A. David, T. Fujii, R. Sharma, K. McGroddy, S. Nakamura, S. P. DenBaars, E. L. Hu, C. Weisbuch, and H. Benisty, "Photonic-crystal gan light-emitting diodes with tailored guided modes distribution," Appl. Phys. Lett. **88**(6), 061124 (2006).

27. J. Shakya, K. Kim, J. Lin, and H. Jiang, "Enhanced light extraction in iii-nitride ultraviolet photonic crystal light-emitting diodes," Appl. Phys. Lett. **85**(1), 142–144 (2004).

28. C.-F. Lai, J.-Y. Chi, H.-H. Yen, H.-C. Kuo, C.-H. Chao, H.-T. Hsueh, J.-F. T. Wang, C.-Y. Huang, and W.-Y. Yeh, "Polarized light emission from photonic crystal light-emitting diodes," Appl. Phys. Lett. **92**(24), 243118 (2008).

29. M.-K. Kwon, J.-Y. Kim, I.-K. Park, K. S. Kim, G.-Y. Jung, S.-J. Park, J. W. Kim, and Y. C. Kim, "Enhanced emission efficiency of ga n/ in ga n multiple quantum well light-emitting diode with an embedded photonic crystal," Appl. Phys. Lett. **92**(25), 251110 (2008).

30. A. David, H. Benisty, and C. Weisbuch, "Optimization of light-diffracting photonic-crystals for high extraction efficiency leds," J. Disp. Technol. **3**(2), 133–148 (2007).

31. H. Benisty, J. Danglot, A. Talneau, S. Enoch, J. M. Pottage, and A. David, "Investigation of extracting photonic crystal lattices for guided modes of gaas-based heterostructures," IEEE J. Quantum Electron. **44**(8), 777–789 (2008).

32. S. Gorsky, R. Zhang, A. Gok, R. Wang, K. Kebede, A. Lenef, M. Raukas, and L. Dal Negro, "Directional light emission enhancement from led-phosphor converters using dielectric vogel spiral arrays," APL Photonics **3**(12), 126103 (2018).

33. S. Gorsky, W. Britton, Y. Chen, J. Montaner, A. Lenef, M. Raukas, and L. Dal Negro, "Engineered hyperuniformity for directional light extraction," APL Photonics **4**(11), 110801 (2019).

34. X.-L. Wang, G.-D. Hao, and N. Toda, "Controlling the directionality of spontaneous emission by evanescent wave coupling," Appl. Phys. Lett. **107**(13), 131112 (2015).

35. H. Chung, C. Zhou, X. Tee, K.-Y. Jung, and P. Bermel, "Hybrid dielectric light trapping designs for thin-film cdznte/si tandem cells," Opt. Express **24**(14), A1008–A1020 (2016).

36. R. Pestourie, C. Pérez-Arancibia, Z. Lin, W. Shin, F. Capasso, and S. G. Johnson, "Inverse design of large-area metasurfaces," Opt. Express **26**(26), 33732–33747 (2018).

37. E. S. Harper, E. J. Coyle, J. P. Vernon, and M. S. Mills, "Inverse design of broadband highly reflective metasurfaces using neural networks," Phys. Rev. B **101**(19), 195104 (2020).

38. H. Chung and O. D. Miller, "Tunable metasurface inverse design for 80% switching efficiencies and 144 angular deflection," ACS Photonics **7**(8), 2236–2243 (2020).

39. C. M. Lalau-Keraly, S. Bhargava, O. D. Miller, and E. Yablonovitch, "Adjoint shape optimization applied to electromagnetic design," Opt. Express **21**(18), 21693–21701 (2013).

40. A. Y. Piggott, J. Lu, K. G. Lagoudakis, J. Petykiewicz, T. M. Babinec, and J. Vučković, "Inverse design and demonstration of a compact and broadband on-chip wavelength demultiplexer," Nat. Photonics **9**(6), 374–377 (2015).

41. L. Su, A. Y. Piggott, N. V. Sapra, J. Petykiewicz, and J. Vuckovic, "Inverse design and demonstration of a compact on-chip narrowband three-channel wavelength demultiplexer," ACS Photonics **5**(2), 301–305 (2018).

42. V. Ganapati, O. D. Miller, and E. Yablonovitch, "Light trapping textures designed by electromagnetic optimization for subwavelength thick solar cells," IEEE J. Photovoltaics **4**(1), 175–182 (2014).

43. S. Molesky, Z. Lin, A. Y. Piggott, W. Jin, J. Vucković, and A. W. Rodriguez, "Inverse design in nanophotonics," Nat. Photonics **12**(11), 659–670 (2018).

44. T. W. Hughes, M. Minkov, I. A. Williamson, and S. Fan, "Adjoint method and inverse design for nonlinear nanophotonic devices," ACS Photonics **5**(12), 4781–4787 (2018).

45. C.-Y. A. Ni and S. L. Chuang, "Theory of high-speed nanolasers and nanoleds," Opt. Express **20**(15), 16450–16470 (2012).

46. D. Schiavon, R. Mroczyński, A. Kafar, G. Kamler, I. Levchenko, S. Najda, and P. Perlin, "Refractive index of heavily germanium-doped gallium nitride measured by spectral reflectometry and ellipsometry," Materials **14**(23), 7364 (2021).

47. P. Campbell and M. A. Green, "Light trapping properties of pyramidally textured surfaces," J. Appl. Phys. **62**(1), 243–249 (1987).

48. A. W. Rodriguez, O. Ilic, P. Bermel, I. Celanovic, J. D. Joannopoulos, M. Soljačić, and S. G. Johnson, "Frequency-selective near-field radiative heat transfer between photonic crystal slabs: a computational approach for arbitrary geometries and materials," Phys. Rev. Lett. **107**(11), 114302 (2011).

49. C. Luo, A. Narayanaswamy, G. Chen, and J. Joannopoulos, "Thermal radiation from photonic crystals: a direct calculation," Phys. Rev. Lett. **93**(21), 213905 (2004).

50. W. Yao, F. Verdugo, R. E. Christiansen, and S. G. Johnson, "Trace formulation for photonic inverse design with incoherent sources," arXiv preprint arXiv:2111.13046 (2021).

51. P. Zhu, "Frustrated total internal reflection in organic light-emitting diodes employing sphere cavity embedded in polystyrene," J. Opt. **18**(2), 025403 (2016).

52. H. Chung and O. D. Miller, "High-na achromatic metalenses by inverse design," Opt. Express **28**(5), 6945–6965 (2020).

53. O. D. Miller, *Photonic design: From fundamental solar cell physics to computational inverse design* (University of California, Berkeley, 2012).

54. S. G. Johnson, M. Ibanescu, M. Skorobogatiy, O. Weisberg, J. Joannopoulos, and Y. Fink, "Perturbation theory for maxwell's equations with shifting material boundaries," Phys. Rev. E **65**(6), 066611 (2002).

55. P. J. Werbos, *The roots of backpropagation: from ordered derivatives to neural networks and political forecasting*, vol. 1 (John Wiley & Sons Press, 1994).

56. D. E. Rumelhart, G. E. Hinton, and R. J. Williams, "Learning representations by back-propagating errors," Nature **323**(6088), 533–536 (1986).

57. S. Ruder, "An overview of gradient descent optimization algorithms," arXiv preprint arXiv:1609.04747 (2016).

58. D. P. Mandic, "A generalized normalized gradient descent algorithm," IEEE Signal Process. Lett. **11**(2), 115–118 (2004).

59. M. Bartholomew-Biggs, *Nonlinear optimization with engineering applications*, vol. 19 (Springer Science & Business Media Press, 2008).

60. S. G. Johnson, "The nlopt nonlinear-optimization package," (2014).

61. A. F. Oskooi, D. Roundy, M. Ibanescu, P. Bermel, J. D. Joannopoulos, and S. G. Johnson, "Meep: A flexible free-software package for electromagnetic simulations by the fdtd method," Comput. Phys. Commun. **181**(3), 687–702 (2010).

62. A. Farjadpour, D. Roundy, A. Rodriguez, M. Ibanescu, P. Bermel, J. D. Joannopoulos, S. G. Johnson, and G. W. Burr, "Improving accuracy by subpixel smoothing in the finite-difference time domain," Opt. Lett. **31**(20), 2972–2974 (2006).

63. I. H. Malitson, "Interspecimen comparison of the refractive index of fused silica," J. Opt. Soc. Am. **55**(10), 1205–1209 (1965).

64. E. D. Palik, *Handbook of optical constants of solids*, vol. 3 (Academic Press, 1998).

65. A. Barker Jr and M. Ilegems, "Infrared lattice vibrations and free-electron dispersion in gan," Phys. Rev. B **7**(2), 743–750 (1973).

66. H. Shim, H. Chung, and O. D. Miller, "Maximal free-space concentration of electromagnetic waves," Phys. Rev. Appl. **14**(1), 014007 (2020).

67. P. Zhu, G. Liu, J. Zhang, and N. Tansu, "Fdtd analysis on extraction efficiency of gan light-emitting diodes with microsphere arrays," J. Disp. Technol. **9**(5), 317–323 (2013).

68. B. Bourdin, "Filters in topology optimization," Int. J. Numer. Meth. Engng. **50**(9), 2143–2158 (2001).

69. M. P. Bendsoe and O. Sigmund, *Topology optimization: theory, methods, and applications* (Springer Science & Business Media Press, 2003).

70. O. Sigmund and K. Maute, "Topology optimization approaches," Struct. Multidisc. Optim. **48**(6), 1031–1055 (2013).

71. S. Wang, P. C. Wu, V.-C. Su, Y.-C. Lai, M.-K. Chen, H. Y. Kuo, B. H. Chen, Y. H. Chen, T.-T. Huang, J.-H. Wang, R.-M. Lin, C.-H. Kuan, T. L. Li, Z. Wang, S. Zhu, and D. P. Tsai, "A broadband achromatic metalens in the visible," Nat. Nanotechnol. **13**(3), 227–232 (2018).

72. D. Sell, J. Yang, S. Doshay, R. Yang, and J. A. Fan, "Large-angle, multifunctional metagratings based on freeform multimode geometries," Nano Lett. **17**(6), 3752–3757 (2017).

73. E. W. Wang, D. Sell, T. Phan, and J. A. Fan, "Robust design of topology-optimized metasurfaces," Opt. Mater. Express **9**(2), 469–482 (2019).